Supplementary Information:
Observation of a topological crystalline insulator phase and topological phase transition in $Pb_{1-x}Sn_xTe$

Su-Yang Xu, Chang Liu, N. Alidoust, M. Neupane, D. Qian, I. Belopolski, J. D. Denlinger, Y. J. Wang, H. Lin, L. A. Wray, G. Landolt, B. Slomski, J. H. Dil, A. Marcinkova, E. Morosan, Q. Gibson, R. Sankar, F. C. Chou, R. J. Cava, A. Bansil, and M. Z. Hasan

This file includes:

Supplementary Figures

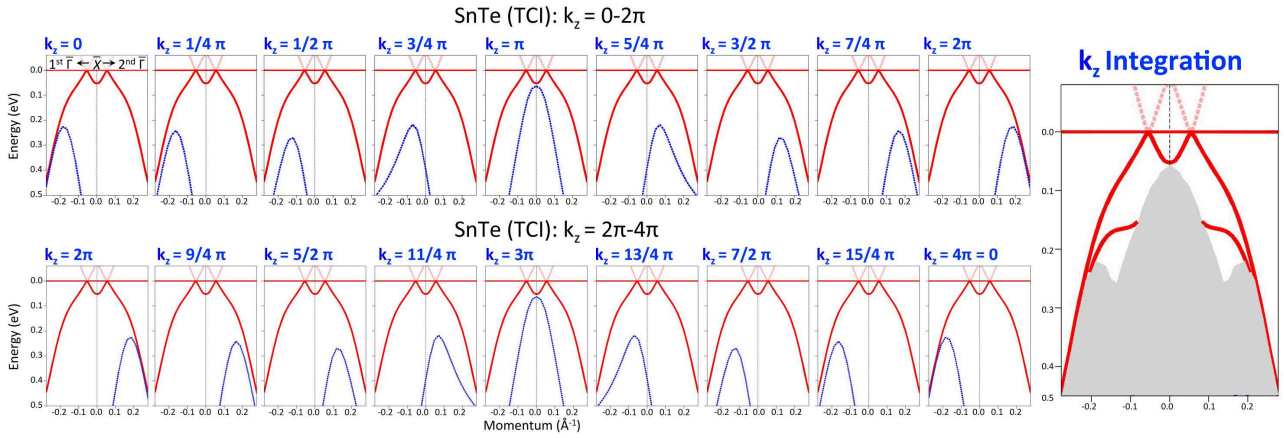

Supplementary Figure 1: **Calculation of bulk band dispersion in SnTe.** Theoretical calculated electronic structure of SnTe is shown along $\bar{\Gamma}$(first surface BZ)$-\bar{X}-\bar{\Gamma}$(second surface BZ) mirror line direction. The SnTe lattice in ideal sodium chloride structure without rhombohedral distortion is used in the calculation. The experimental lattice constants of SnTe with the value of 6.327 Å are used. Therefore the TCI surface states are realized in the calculation. The red and blue lines correspond to the TCI surface states and the bulk bands respectively. The dispersion of the surface states is found to be independent of the k_z values, whereas the bulk bands are found to show strong k_z dispersion with a k_z period of 4π. Right panel: Theoretical calculation of SnTe surface states and projection of band bands, showing how the surface states are connected to the bulk bands. The bulk band projection is the bulk valence band integrated over the entire k_z range from $k_z = 0$ to $k_z = 4\pi$.

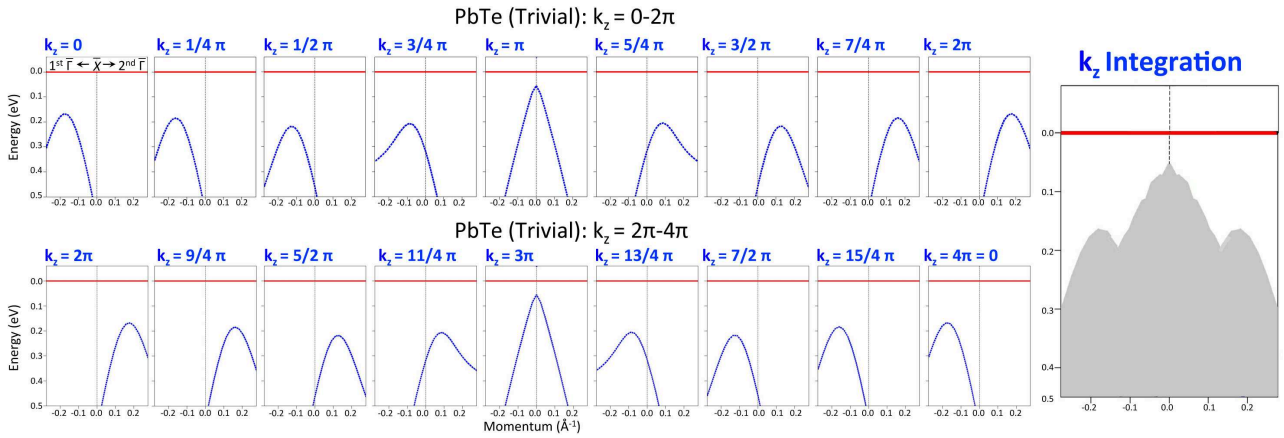

Supplementary Figure 2: **Calculation of bulk band dispersion in PbTe.** Theoretical calculated electronic structure of PbTe is shown along $\bar{\Gamma}$(first surface BZ)$-\bar{X}-\bar{\Gamma}$(second surface BZ) mirror line direction. The experimental lattice constant of PbTe with the value of 6.46 Å in ideal sodium chloride are used in the PbTe band structure calculation. The trivial insulator phase is realized in PbTe and no surface states is found in the calculation. The blue lines correspond to the bulk bands at different k_z values. The bulk bands are found to show strong k_z dispersion with a period of 4π. Right panel: Theoretical calculation of PbTe projection of band bands. The bulk band projection is the bulk valence band integrated over the entire k_z range from $k_z = 0$ to $k_z = 4\pi$.

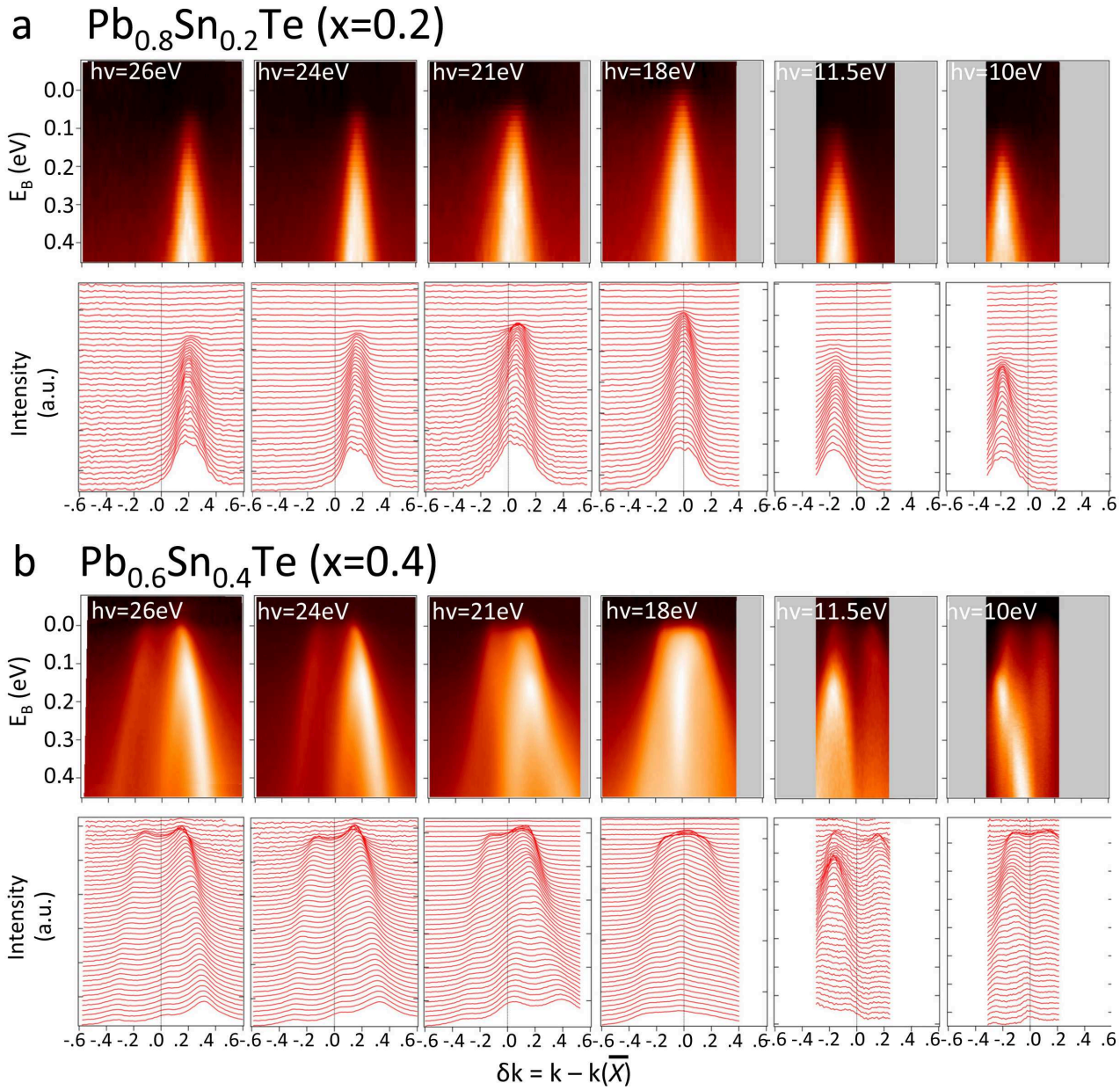

Supplementary Figure 3: **Incident photon energy dependence study of $Pb_{0.8}Sn_{0.2}Te$ and $Pb_{0.6}Sn_{0.4}Te$. a,** The ARPES dispersion maps and corresponding momentum distribution curves (MDCs) along the $\bar{\Gamma}$(first surface BZ)$-\bar{X}-\bar{\Gamma}$(second surface BZ) mirror line direction at different incident photon energies for the non-inverted composition $Pb_{0.8}Sn_{0.2}Te$. **b,** The ARPES dispersion maps and corresponding momentum distribution curves (MDCs) along the $\bar{\Gamma}-\bar{X}-\bar{\Gamma}$ mirror line direction at different incident photon energies for the inverted composition $Pb_{0.6}Sn_{0.4}Te$. For the non-inverted $x = 0.2$ sample, no surface states on the Fermi level is observed for all the incident photon energy values applied under the same experimental conditions and setups. The k_z evolution (dispersion) of the bulk valence band at different k_z values (different incident photon energies) is

Supplementary Figure 3: (Previous page.) in qualitative agreement with the theoretical calculation results shown above. For the inverted $x = 0.4$ sample, a pair of metallic states is observed on the opposite sides of each $\bar{X}$ point. The dispersion of the metallic states on the Fermi level is found to show no observable change upon varying the incident photon energy. The bulk valence band is observed to be a single hole-like band below the Fermi level at each photon energy, which shows strong dispersion with respect to the incident photon energy.

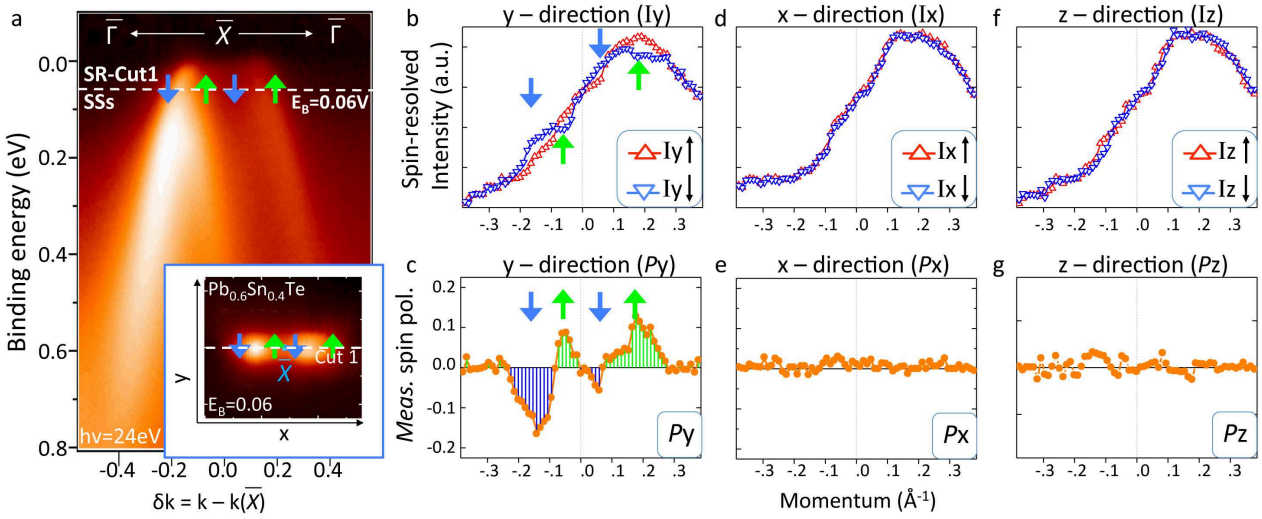

Supplementary Figure 4: **Spin measurements near the surface state Fermi level. a,** ARPES measured dispersion map along the $\bar{\Gamma} - \bar{X} - \bar{\Gamma}$ mirror line direction. The white dotted line shows the binding energy chosen for the spin-resolved measurement of SR-Cut 1. SR-Cut1 is at binding energy near the Fermi level ($E_{\rm B} = 0.06$ eV), and thus it measures the spin polarization of the surface states. Inset shows the momentum space direction of SR-Cut 1 in the (k_x, k_y) momentum space plane on top of the measured iso-energetic contour of the surface states at $E_{\rm B} = 0.06$ eV. The blue and green arrows represent the measured spin polarization configuration of SR-Cut1. **b-c,** The spin-resolved intensity along $\pm\hat{y}$ direction, and the $\hat{y}$ component of the measured spin polarization of SR-Cut 1. In total four spin vectors pointing along the $\pm\hat{y}$ direction are clearly revealed by the spin-resolved measurements. **d-e, and f-g,** Same as **b,c,** but for the $\hat{x}$ and $\hat{z}$ components of the spin, respectively. No significant $\hat{x}$ and $\hat{z}$ components of spin polarization is observed.

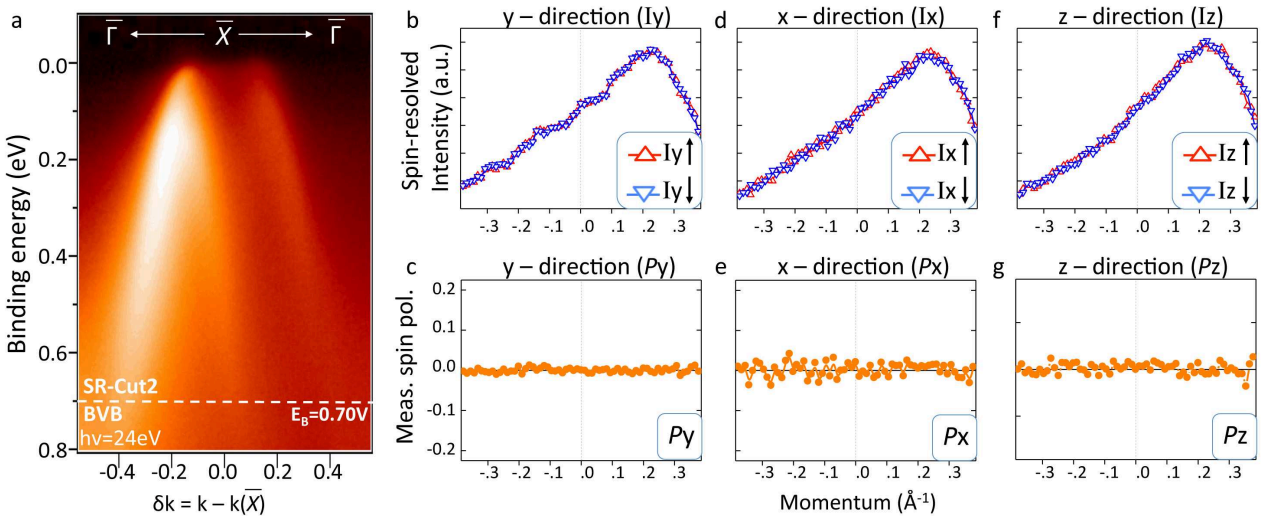

Supplementary Figure 5: **Spin measurements at high binding energy (bulk valence bands). a,** ARPES measured dispersion map along the $\bar{\Gamma}-\bar{X}-\bar{\Gamma}$ mirror line direction. The white dotted line shows the binding energy chosen for the spin-resolved measurement of SR-Cut 2. SR-Cut 2 is at high binding energy far away from the Fermi level ($E_{\mathrm{B}} = 0.70$ eV), and thus it measures the spin polarization of the bulk valence bands. **b-c, d-e, and f-g** The spin-resolved intensity and the measured spin polarization of SR-Cut 2 along the $\hat{y}$, $\hat{x}$, and $\hat{z}$ directions, respectively. No significant spin polarization is observed for SR-Cut 2 (the bulk valence bands).

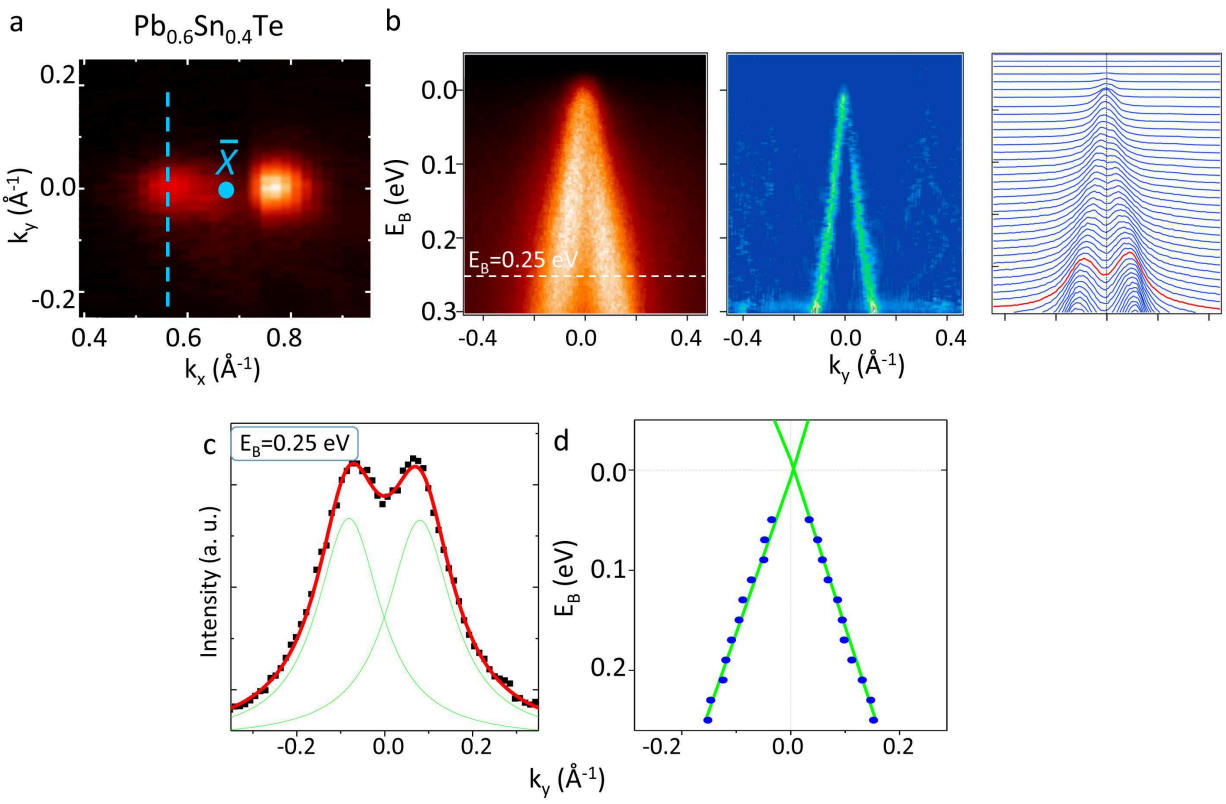

Supplementary Figure 6: **Surface state lineshape. a,** Fermi surface mapping zoomed-in in the vicinity of an $\bar{X}$ point. **b,** Dispersion map, second derivative analysis, and the corresponding momentum distribution curves of the surface states along momentum space cut direction defined by the blue dotted lines in **a**. The momentum distribution curve at $E_{\mathrm{B}} = 0.25$ eV is highlighted in red. **c,** The Lorentzian fitting of the momentum distribution curve at $E_{\mathrm{B}} = 0.25$ eV. **d,** The dispersion data points (E_{B}, k) of the surface states are obtained from the Lorentzian fitting of the momentum distribution curves at different binding energies and shown by the solid blue circles. Then the surface state dispersion is fitted by linear function in order to obtain the velocity of the surface states.

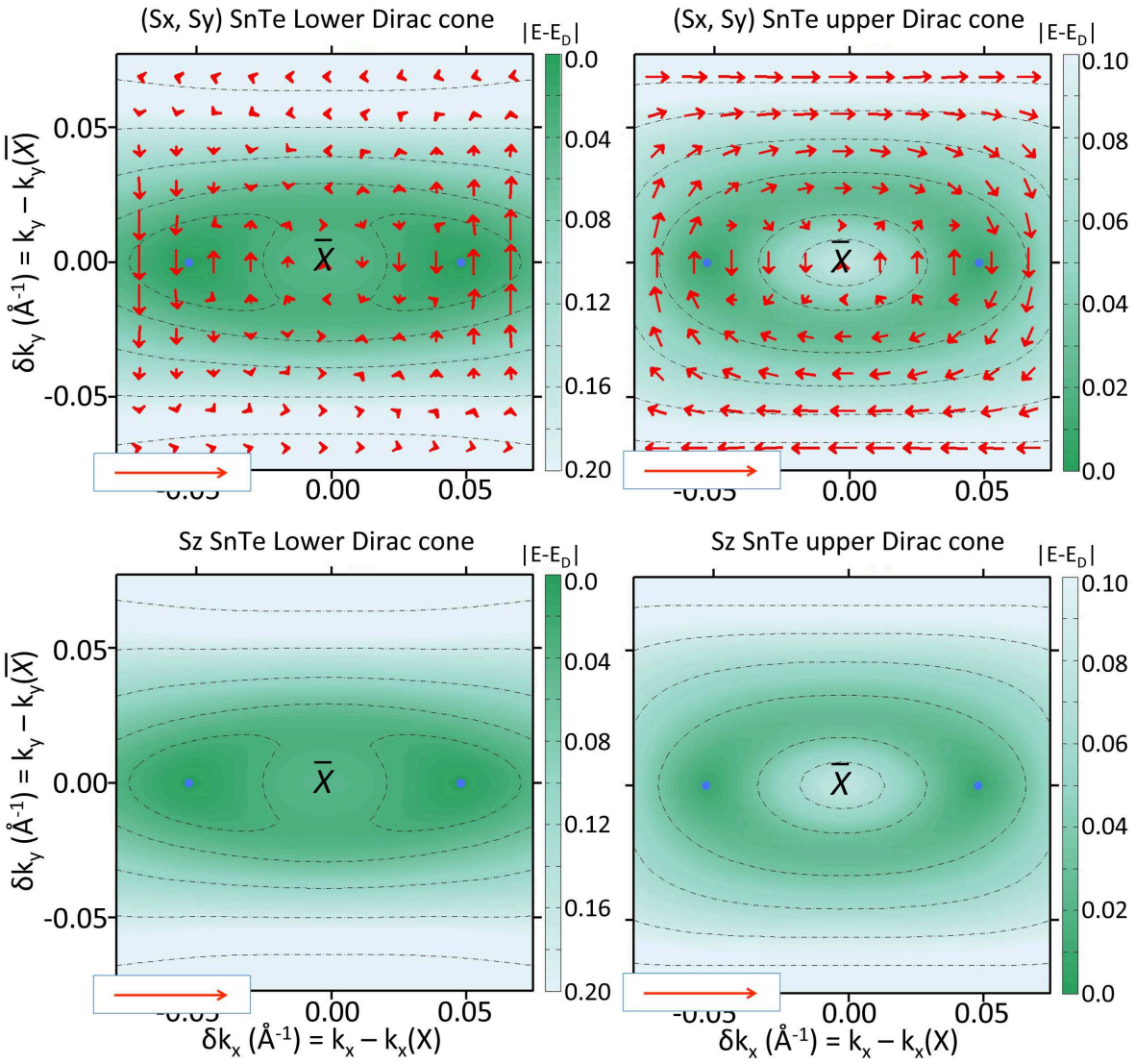

Supplementary Figure 7: **Spin texture of the (001) SnTe surface states in the vicinity of an $\bar{X}$ point based on first-principles calculation.** The in-plane components (P_x, P_y) of the SnTe surface states spin texture. The red arrows represent the spin polarization at the corresponding momentum space location. The direction and the length of the arrows show the direction and the magnitude of the spin polarization, respectively. The insets represent the length of the unit spin vector with spin polarization of 1 (100%). The out-of-plane component is found to be zero throughout the calculated $(E_{\mathrm{B}}, k_x, k_y)$ range. The two blue dots denote the two Dirac points on the opposite sides of the $\bar{X}$ point. The color scale shows the energy of the surface states' contours with respect to the Dirac point energy (E_{D}). The black dotted lines show the iso-energetic contours of the surface states at different energies. The left panel shows the spin texture below the Dirac points (lower Dirac cones), and the right panel shows the spin texture above the Dirac points (upper Dirac cones).

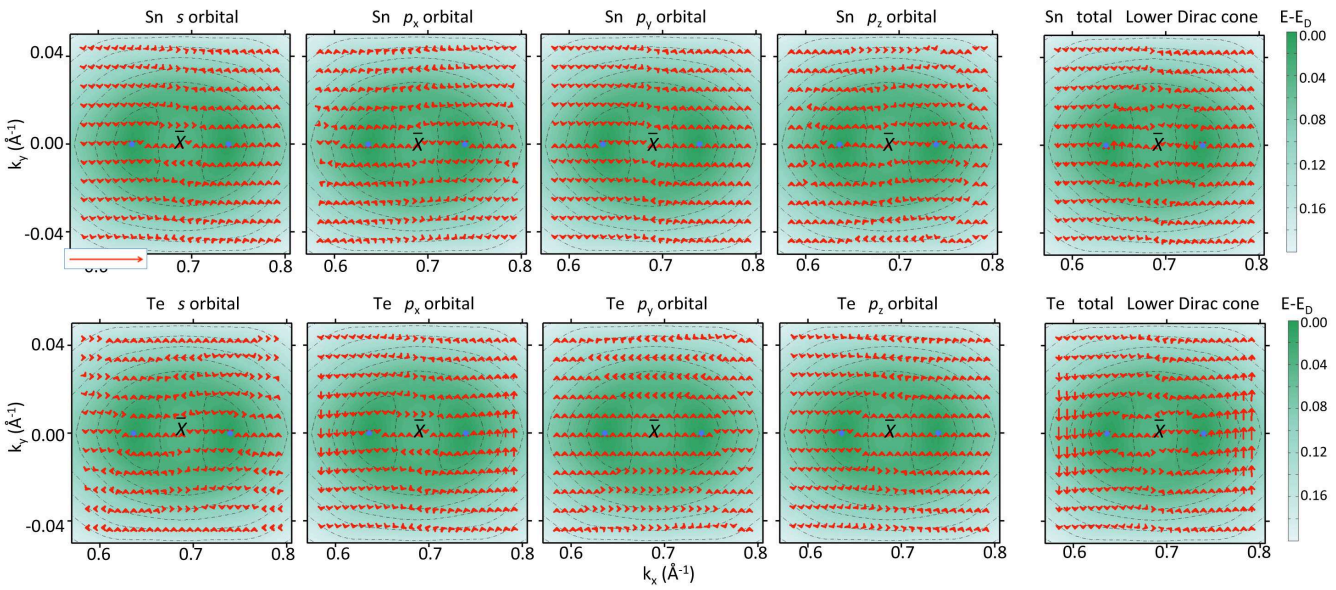

Supplementary Figure 8: **Calculated spin texture decomposed into their orbital origins.** The spin of s, p_x, p_y, and p_z orbitals of Sn and Te atoms are shown for the lower Dirac cones of the surface states. The inset represents the length of the unit spin vector with spin polarization of 1 (100%) for all panels. The two blue dots denote the two Dirac points on the opposite sides of the $\bar{X}$ point. The color scale shows the energy of the surface states' contours with respect to the Dirac point energy (E_{D}). The black dotted lines show the iso-energetic contours of the surface states at different energies.

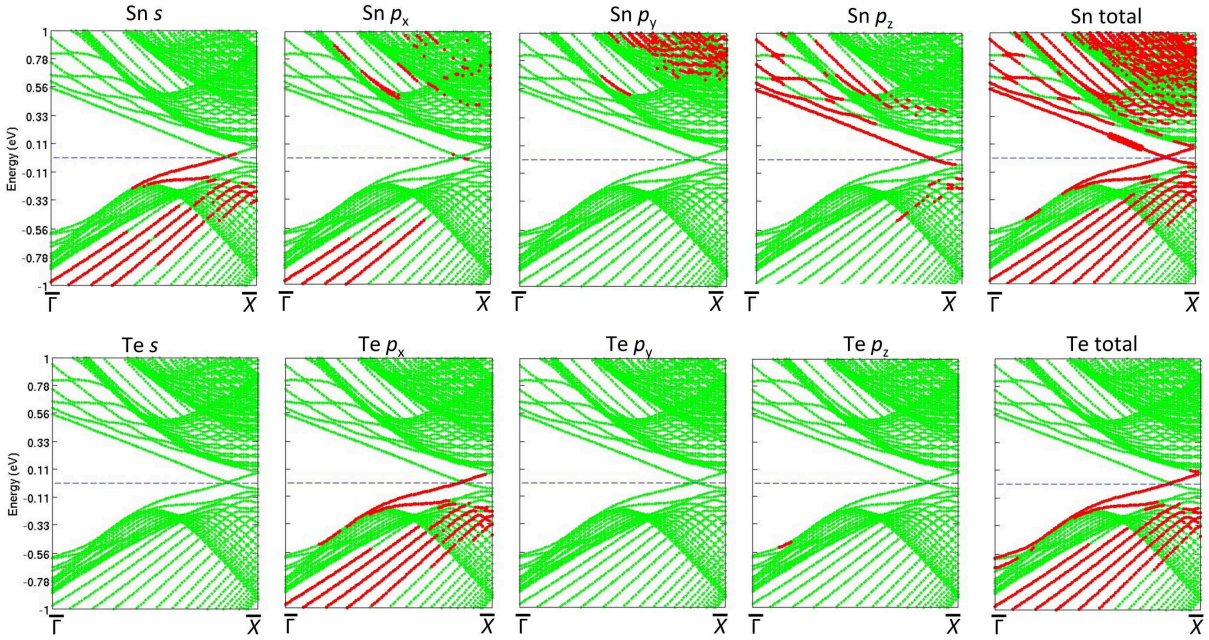

Supplementary Figure 9: **Orbital projections of the SnTe (001) surface states.** The red lines denote that the corresponding electronic states have a strong contribution (weight) from certain orbitals, whereas the green lines denote that the corresponding electronic states have a very small contribution (weight) from certain orbitals.

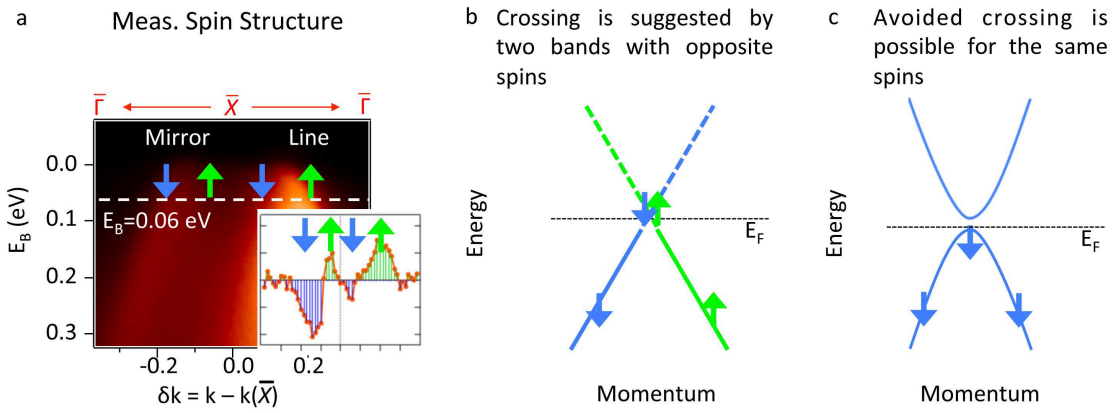

Supplementary Figure 10: **Spin polarization profile and Dirac crossing.** **a,** The spin polarization of the surface states along the $\bar{\Gamma} - \bar{X} - \bar{\Gamma}$ mirror line direction revealed by our spin-resolved measurement SR-Cut 1. **b,** Theoretically, two spin singlet bands with opposite spin directions can only cross each other. **c,** Avoided crossing is allowed for band with the same spin flavor, or a spin degenerate band.

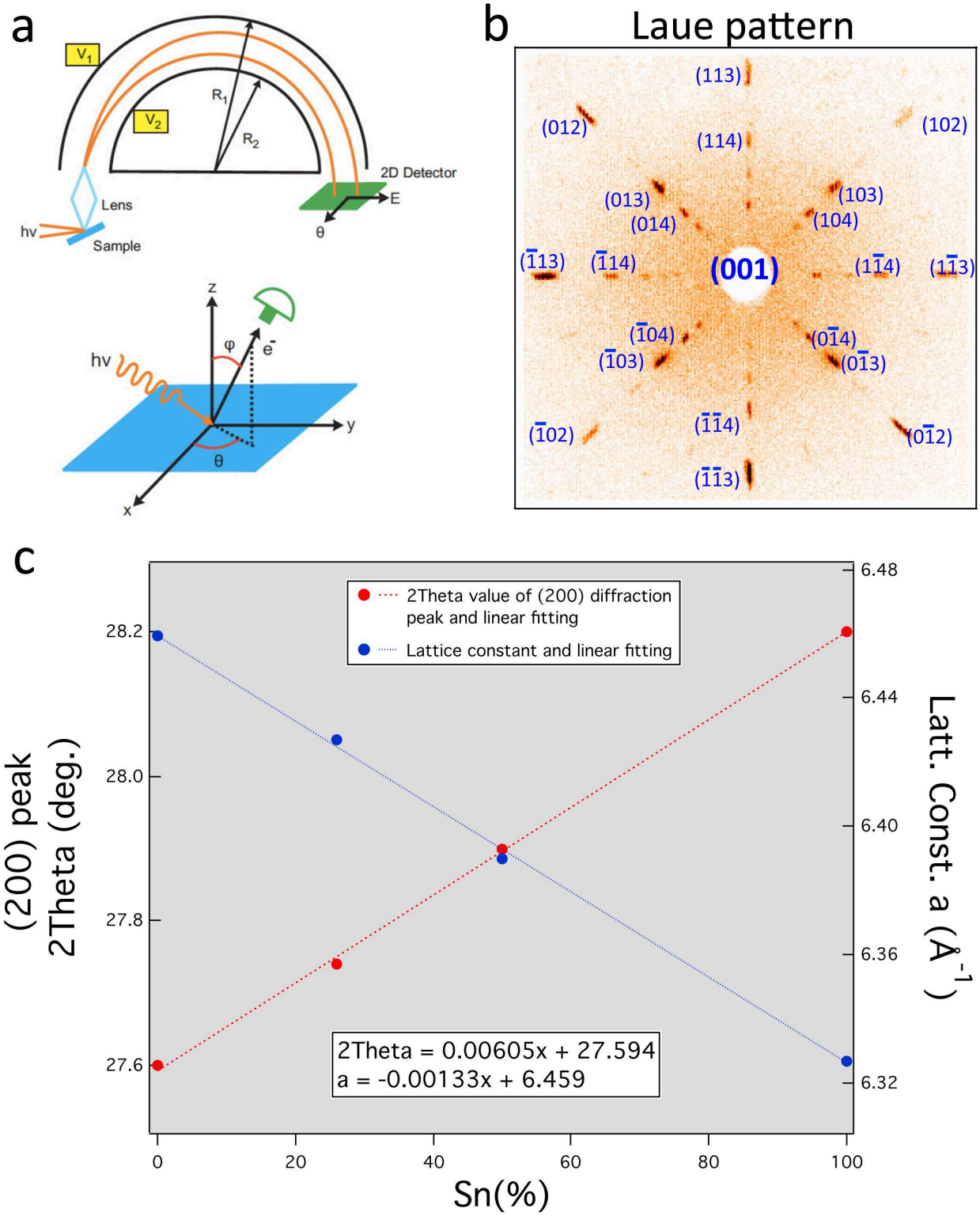

Supplementary Figure 11: **Scattering geometry and sample characterization. a,** Top: The electron analyzer setup used to measure emitted photoelectrons from the sample surface.

Supplementary Figure 11: (Previous page.) The two hemispheres detect the electrons to produce a 2D image of energy vs momentum in one shot. Bottom: The geometry of the detector relative to the sample surface. The momentum of the electron inside the sample can be extracted from the measured values of E_{kin}, θ and ϕ. **b,** X-ray Laue diffraction pattern of a representative $Pb_{0.6}Sn_{0.4}Te$ sample used for ARPES experiments. The Miller indices are noted for the diffraction peaks in Laue pattern, which reveals that the cleavage surface of the crystal is perpendicular to the [001] vertical crystal axis. **c,** The 2Theta values of the (200) Bragg peak (the sharpest and most intensive peak for X-ray diffraction on $Pb_{1-x}Sn_xTe$ [44, 45], also see Supplementary Figure 12a) and the corresponding lattice constant values for PbTe ($x = 0\%$), $Pb_{0.74}Sn_{0.26}Te$ ($x = 26\%$), $Pb_{0.50}Sn_{0.50}Te$ ($x = 50\%$), and SnTe ($x = 100\%$) obtained from Ref. [44-47] respectively. Linear fittings are applied to the data points, from which we obtain 2Theta $= 0.00605x + 27.594$ and $a = -0.00133x + 6.459$.

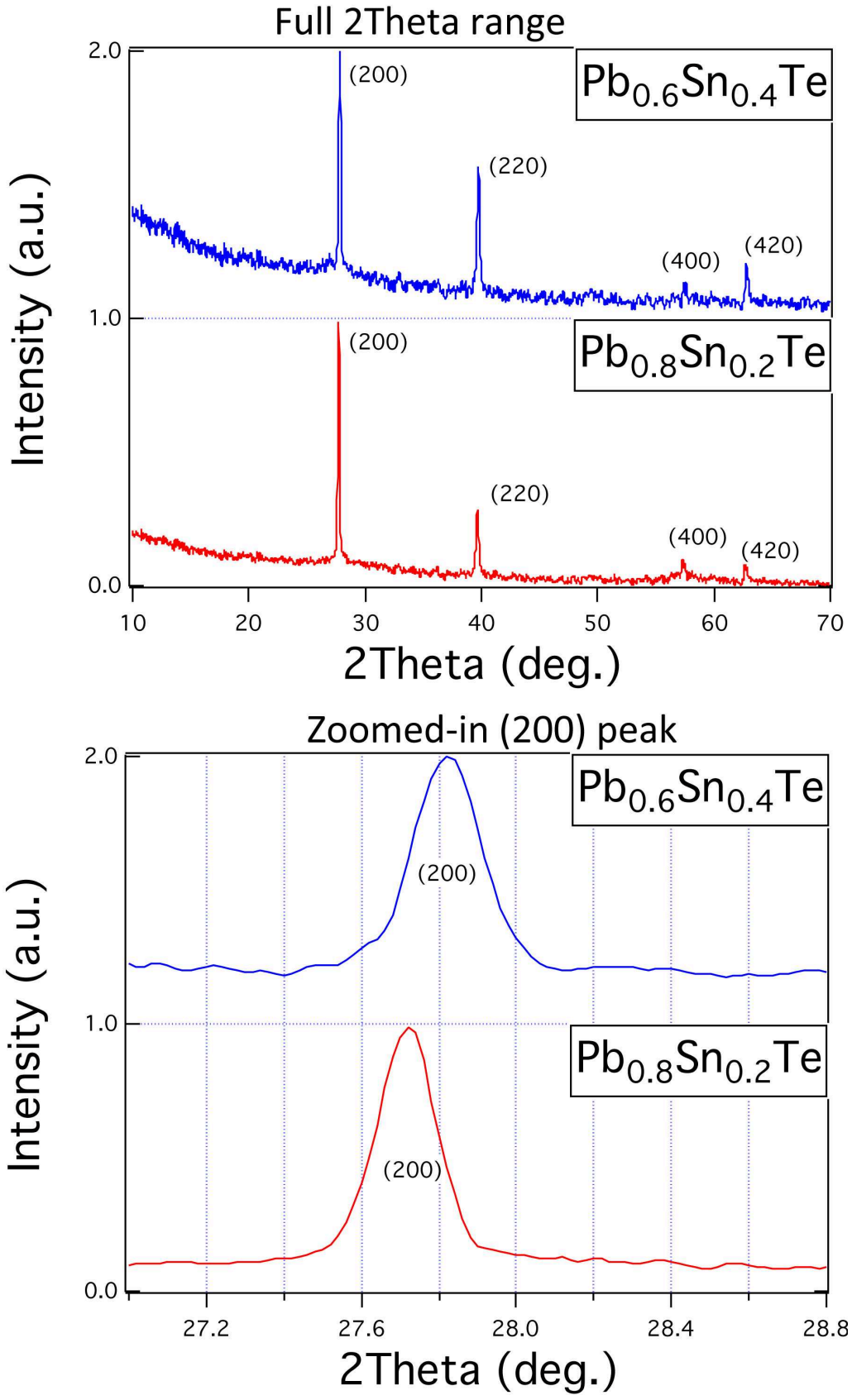

Supplementary Figure 12: **X-ray diffraction measurements on two representative compositions.**

Supplementary Figure 12: (Previous page.) **a,** X-ray diffraction measurements on the two representative compositions. The intensity of the XRD measurements is normalized (maximum intensity to be 1). The XRD data of $Pb_{0.6}Sn_{0.4}Te$ is offset by 1 with respect to that of $Pb_{0.8}Sn_{0.2}Te$. The corresponding indices of the Bragg peaks are noted. **b,** The diffraction data zoomed-in in close vicinity of the (200) Bragg peak for the two compositions. The 2Theta values of the (200) Bragg peak are found to be 27.73 deg and 27.83 deg for the two compositions. Using the formula $2\text{Theta} = 0.00605x + 27.594$ obtained from linear fittings in Supplementary Figure 11c, we obtain that these 2Theta values correspond to x values of $x = 0.22$ (for the nominal concentration $x_{\text{nom}} = 0.20$ samples) and $x = 0.39$ (for the nominal concentration $x_{\text{nom}} = 0.36$ samples). In the paper we note the chemical compositions as $Pb_{0.8}Sn_{0.2}Te$ and $Pb_{0.6}Sn_{0.4}Te$.

Supplementary Discussion

- **The topological distinction between TI and TCI phases**

  - **TCI vs. TI / Even vs. Odd number of band inversions:** It is important to note that the $Pb_{1-x}Sn_xTe$ system contains an even number of inversions [9]. Traditionally even number of band inversions are believed to be topologically trivial, and only odd number of inversions are believed to give rise to topological insulator states [2]. For this reason, although the $Pb_{1-x}Sn_xTe$ system has long been known to contain an even number of inversions, they were believed to be trivial insulators. (see Ref. [2]). Since the much studied Z_2 TIs can only be realized via odd number of inversions, thus the even number inversions in the SnTe system determines that such system is topologically distinct from both the TI phase and the trivial band insulator phase, which means TCI is a new phase of topological matter.

  - **Irrelevance of Time-Reversal Symmetry Protection:** The topological distinction between TCI and TI can be directly seen from our ARPES measured surface states. For example, Fig. 5 in the maintext shows an ARPES comparison between a Z_2 (Kane-Mele) TI $GeBi_2Te_4$ and our new $Pb_{0.6}Sn_{0.4}Te$ samples. As shown in Fig. 5 of the maintext, $GeBi_2Te_4$ belongs to the well-understood single Dirac cone topological insulator, which is topologically the same as the famous Bi_2Se_3 or Bi_2Te_3 systems. $GeBi_2Te_4$ has only one surface state (odd number), which is found to enclose the time-reversal invariant momenta (TRIM) or the Kramers point (the $\bar{\Gamma}$ point). For this reason, the single Dirac cone surface state in $GeBi_2Te_4$ (also Bi_2Se_3, Bi_2Te_3, and all other Z_2 TI systems) is topologically protected by time-reversal symmetry. In sharp contrast, in the $Pb_{0.6}Sn_{0.4}Te$ system, none of the surface states are found to enclose any of the time-reversal invariant momenta (TRIM). Thus the surface states in the $Pb_{0.6}Sn_{0.4}Te$ system are irrelevant to time-reversal symmetry type of protection. The topological protection in the case of $Pb_{0.6}Sn_{0.4}Te$ is a result of the mirror (spatial) symmetries of the crystal, as theoretically predicted by Ref. [15]. One relevant experimental evidence for the mirror protection is that all of the observed surface states are

located on the mirror line momentum space directions ($\bar{\Gamma} - \bar{X} - \bar{\Gamma}$).

- **Spin polarization, Dirac crossing and gapless nature**

  Here we provide one experimental observation relevant to the Dirac crossing and gapless nature: the spin polarization profile. As shown in Supplementary Figure 10, for two electronic bands with opposite spin directions, crossing is the only fate. The avoided crossing and gap behavior is only allowed if the bands have the same spin flavor or they are spin degenerate. Here we show that at energy level 60 meV below the chemical potential (thus about 60 ± 20 meV around the Dirac point), the two branches of each surface state cone show the expected opposite spin directions. It has been recently experimentally shown that the spin texture of the Dirac surface states will be strongly disturbed when a gap is opened at the Dirac point [38]. The energy scale where the spin texture is disturbed roughly corresponds to the gap value [38]. Therefore, by showing a helical spin structure at about 60 ± 20 meV around the Dirac point in Supplementary Figure 4c and Supplementary Figure 10a, we can safely exclude a gap value of 50 meV. However, whether there is a ≤ 10 meV gap or not in our surface states still need further studies.

Supplementary Methods

- **Laue measurements**

  The surface cleavage termination is determined by X-ray diffraction measurements on the cleaved samples after ARPES measurements. Supplementary Figure 11b shows a representative Laue measurement on the $Pb_{0.6}Sn_{0.4}Te$ ($x = 0.4$) sample. The Miller indices are noted for the diffraction peaks in Laue pattern, which reveals that the cleavage surface of the crystal is perpendicular to the [001] vertical crystal axis. The (001) surface termination determined here from Laue results is consistent with the four-fold symmetry of the ARPES Fermi surfaces and the size of the surface BZ in ARPES measurements.

- **X-ray diffraction measurements**

  As shown in Supplementary Figure 12 for our XRD measurements on the two representative compositions, the 2Theta values of the (200) Bragg peak are found to be 27.73 deg (for the nominal concentration $x_{\mathrm{nom}} = 0.20$ samples, noted as $Pb_{0.8}Sn_{0.2}Te$ in the maintext) and 27.83 deg (for the nominal concentration $x_{\mathrm{nom}} = 0.36$ samples, noted as $Pb_{0.6}Sn_{0.4}Te$ in the maintext). Using the linear fitting above, these 2Theta values correspond to x values of $x = 0.22$ (for the nominal concentration $x_{\mathrm{nom}} = 0.20$ samples) and $x = 0.39$ (for the nominal concentration $x_{\mathrm{nom}} = 0.36$ samples). In the paper we note the chemical compositions as $Pb_{0.8}Sn_{0.2}Te$ and $Pb_{0.6}Sn_{0.4}Te$.

- **Incident photon energy dependence study on $Pb_{1-x}Sn_xTe$**

  As a qualitative guide to the ARPES incident photon energy dependence measurements, here we show the first-principles calculated bulk bands k_z dispersion of the two end compounds inverted SnTe (Supplementary Figure 1) and non-inverted PbTe (Supplementary Figure 2) respectively.

  Now we present comparative incident photon energy dependence studies between the inverted $Pb_{0.6}Sn_{0.4}Te$ samples and the non-inverted $Pb_{0.8}Sn_{0.2}Te$ samples under the identical experimental conditions and setups (beamline, incident photon energy values, incident light polarization, sample surface preparation procedure, etc.) as shown in Supplementary Figure 3. A pair of surface states without observable k_z dispersion

is observed in the inverted $x = 0.4$ samples but absent in the non-inverted $x = 0.2$ samples. no surface state on the Fermi level is observed for all the incident photon energy applied under the same experimental conditions and setups as shown in Supplementary Figure 3a. The k_z evolution (dispersion) of the bulk valence band at different k_z values (different incident photon energies) is in qualitative agreement with the theoretical calculation results shown above. The incident photon energy range from 26 eV to 10 eV shown in Supplementary Figure 3 corresponds to a wide k_z range from 1.8π to 0.1π, which corresponds to going from the top of the bulk BZ to the center of the bulk BZ.

- **Fitting results of the experimental chemical potential with respect to the Dirac point energy**

  We apply a linear fitting to the ARPES dispersion near the Fermi level along Cut 2 in the maintext, which enables us to extract the velocity of the surface states, as well as the chemical potential (E_{F}) with respect to the Dirac point energy (E_{D}).

  - Supplementary Figure 6a shows the Fermi surface mapping zoomed-in in the vicinity of an $\bar{X}$ point. The blue dotted line defines a momentum space cut direction (which is the same as Cut 2 in Fig. 3 of the maintext).
  - Supplementary Figure 6b shows the dispersion map and the corresponding momentum distribution curves (MDCs) along the momentum space cut defined by the blue dotted line in Supplementary Figure 6a.
  - The MDC is the ARPES measured intensity distribution along the momentum axis at a fixed binding energy E_{B}. For example, the white solid line in Supplementary Figure 6b is at binding energy $E_{\mathrm{B}} = 0.25$ eV and the corresponding MDC is highlighted in red in the MDC panel in Supplementary Figure 6b.
  - We fit the MDCs by two Lorentzian peaks. We take the MDC Lorentzian fitting at $E_{\mathrm{B}} = 0.25$ eV as an example, as shown in Supplementary Figure 6c. The Lorentzian peak position reveals the momentum location of each branch of the Dirac surface states at $E_{\mathrm{B}} = 0.25$ eV.
  - By performing such fitting at different binding energies, we obtain the dispersion of the surface states, namely (E_{B}, k). The solid blue circles in Supplementary

Figure 6E show the obtained dispersion data points of the surface states from $E_{\mathrm{B}} = 0.25$ eV to $E_{\mathrm{B}} = 0.05$ eV with a binding energy step of $\Delta E_{\mathrm{B}} = 0.02$ eV.

- Then we fit the surface states' dispersion data points by a linear function. For the two branches of the surface state cone we obtain the following: for the branch with positive slope, we have $E_{\mathrm{B}} = (2.68(\pm 0.07)\mathrm{eV}\cdot\text{Å})\cdot k + 0.008(\pm 0.009)\mathrm{eV}$. And for branch with negative slope, we have $E_{\mathrm{B}} = (-2.88(\pm 0.08)\mathrm{eV}\cdot\text{Å})\cdot k - 0.010(\pm 0.008)\mathrm{eV}$. Thus, the linear fittings of both branches give the velocity (the absolute value of the slope) of the Dirac cone to be around 2.8 eV·Å. The Dirac point energy E_{D} is given by the binding energy intercept ($E_{\mathrm{B}}(k = 0)$) of the linear fitting, which is 0.008 eV and -0.010 eV for each fitting respectively. This means the Dirac point energy E_{D} implied by the fitting of the positive slope branch is 0.008 eV below the chemical potential E_{F}, whereas the Dirac point energy E_{D} implied by the fitting of the negative slope branch is 0.010 eV above the chemical potential E_{F}.
- In the maintext, we report a surface state velocity of 2.8 eV·Å along this momentum space cut direction (Cut 2 in Fig. 3 of the maintext). Furthermore the chemical potential with respect to the Dirac point is found to be $E_{\mathrm{F}} = E_{\mathrm{D}} \pm 0.02$ eV

- **Spin-resolved measurements on $\mathbf{Pb_{0.6}Sn_{0.4}Te}$**

  Here we show systematic spin dataset of these measurements for all three components of the spin polarization vector. The $\hat{x}$, $\hat{y}$ directions for spin polarization vectors are defined in the inset of Supplementary Figure 4a. And the $\hat{z}$ direction follows the right-hand rule. The P_x, P_y and P_z measurements for SR-Cut 1 and SR-Cut 2 are shown in Supplementary Figure 4 and Supplementary Figure 5. As discussed in the main paper, in total four in-plane tangential (P_y) spins are revealed by these polarization measurements (Supplementary Figure 4c) on the surface states. We note that the magnitude of the spin polarization is between $10\% - 20\%$, which is smaller than the typically observed 40% net spin polarization of the Z_2 topological insulator surface states [48]. In fact the $10\% - 20\%$ spin polarization in our $x = 0.4$ samples is found to be consistent with the first-principles based spin texture calculation on SnTe surface states (see below). As shown in Supplementary Figure 4c, the polarization magnitude

of the inner two branches are found to be smaller as compared to that of the outer two branches. This can be understood by two independent reasons: First, since the inner two branches are close to each other in momentum space, their polarization signal can intermix with each other due to the finite momentum resolution of the spin-resolved measurements (the momentum resolution is about 3% of the surface BZ which corresponds to roughly 0.04Å^{-1}). Second, the smaller polarization of the inner two branches is even observed in our calculation on SnTe (see below). This effect is related to the anisotropy of the surface states and the hybridization of the two adjacent Dirac cones.

- **Spin texture calculation of SnTe**

  The spin texture of SnTe is calculated using VASP first-principles method. We have assumed the SnTe lattice in ideal sodium chloride structure without rhombohedral distortion. The calculated spin texture of the SnTe surface states is shown in Supplementary Figure 7 for the lower and upper Dirac cone, respectively. The out-of-plane component of the spin texture is found to be zero. We compare the calculated spin texture with the spin polarization measurements shown above: Along the $\bar{\Gamma} - \bar{X} - \bar{\Gamma}$ mirror line direction ($k_y = 0$ in Supplementary Figure 7a), both theoretical calculations in Supplementary Figure 7a (low Dirac cone) and spin measurements in Supplementary Figure 4c reveal in total 4 spins with alternating directions in going along the mirror line. The magnitude of the spin polarization in calculation is found to range 10% to 30%, which is consistent with the experiments in Supplementary Figure 4c. The inner two spins close to the $\bar{X}$ point are found to have smaller polarization as compared to the outer two, which is also in agreement with the experimental results in Supplementary Figure 4c.

  In order to better understand the spin texture, we also calculate the atomic orbital contribution of the spin texture. For the (001) surface, as shown in Supplementary Figure 9.

Supplementary References

[44] Bouad, N. *et al.* Neutron powder diffraction study of strain and crystallite size in mechanically alloyed PbTe. *J. Solid State Chem.* **173**, 189-195 (2003).

[45] Ishida, A., Aoki, M. Fujiyasu, H. Sn diffusion effects on x-ray diffraction patterns of $Pb_{1-x}Sn_xTe$ -$PbSe_yTe_{1-y}$superlattices. *J. Appl. Phys.* **58**, 797-801 (1985).

[46] Yakimova, R. T., Trifonova, E. P., Karagiozov, L. & Petrov, S. Structural and electrical characteristics of iodidely synthesized $Pb_{1-x}Sn_xTe$ crystals. *S. Cryst. Res. Technol.* **19**, K109-K112 (1984).

[47] Scheer, M., McCarthy, G., Seidler, D. & Boudjouk, P. North Dakota State Univ., Fargo, ND, USA., ICDD Grant-in-Aid (1994).

[48] Hsieh, D. *et al.* A tunable topological insulator in spin helical Dirac transport regime. *Nature* **460**, 1101-1105 (2009).

Correspondence and requests for materials should be addressed to M.Z.H. (Email: mzhasan@princeton.edu).